مركز الأكاديمية للنشر
ACADEMY Publishing Center

RESD
Renewable Energy and Sustainable Development Journal

ISSN 2356-8569

Volume 9
Issue 2
December 2023

indexed in
Scopus

Academy Publishing Center
Journal of Renewable Energy and Sustainable Development (RESD)

Indexed in

Scopus https://www.scopus.com/sourceid/21101163025

RESD
Volume 9, Issue 2, December 2023
p-ISSN: 2356-8518 Print Version
e-ISSN: 2356-8569 Online Version

http://apc.aast.edu

Arab Academy for Science, Technology, and Maritime Transport, AASTMT Abu Kir Campus, Alexandria, EGYPT
P.O. Box: Miami 1029
Tel: (+203) 5622366/88 – EXT 1069 and (+203) 5611818
Fax: (+203) 5611818
Web Site: http://apc.aast.edu

RESD Journal of Renewable Energy and Sustainable Development

Renewable Energy and Sustainable Development (RESD) is a biannual international peer-reviewed journal, which presents a global forum for dissemination of research articles, case studies and reviews focusing on all aspects of renewable energy and its role in sustainable development. The topics of focal interest to RESD include, but are not limited to, all aspects of wind energy, wave/tidal energy, solar energy, as well as energy from biomass and biofuel. The integration of renewable energy technologies in electrical power networks and smart grids is another topic of interest to RESD. Experimental, computational and theoretical studies are all welcomed to RESD.

Sustainable development is a multidisciplinary advancing to the center of energy research with the declaration of UN millennium development goals for the first time in 2000, and continued to constitute a challenge in energy technologies in the past decade. RESD is mainly interested in case studies of sustainable development and its relation to transition economies in the Middle East, Africa, Asia and Oceania.

RESD has an outstanding editorial board of eminent scientists, researchers and engineers who contribute and enrich the journal with their vast experience in different fields of interest to the journal. The journal is open-access with a liberal Creative Commons Attribution-Non Commercial-4.0 International License. Which preserves the copyrights of published materials to the authors and protects it from unauthorized commercial use or derivation. The journal is financially supported by Arab Academy for Science, Technology and Maritime Transporting in order to maintain quality open-access source of research papers on renewable energy and sustainable development.

Editorial Committee

Advisory Board

Administrative Board

Contents

P.32 **2d Solar Thermal Direct Absorption Comparison Between Gold And Silver Nanoparticle**
Abdul-Mubarak Yussif Yidana

P.42 **Computational Simulation Study of the Impact of Isotropic GDL Thermal Conductivity on PEMFC Characteristics**
Mahmut Kaplan

Journal of Renewable Energy and Sustainable Development (RESD) Volume 9, Issue 2, December 2023 - ISSN 2356-8569
http://dx.doi.org/10.21622/RESD.2023.09.2.032

Received on, 06 May 2023 Accepted on, 23 September 2023 Published on, 30 October 2023

2d Solar Thermal Direct Absorption Comparison Between Gold And Silver Nanoparticle

Abdul-Mubarak Yussif Yidana

[1]Bachelor's degree in Mechanical Engineering from SRM University AP, in India

yidanam@gmail.com

ABSTRACT

In recent years, the application of nanoparticles for direct thermal absorption in solar energy technology has emerged as a transformative advancement, showing significant potential compared to traditional solar collectors. In this research, nanofluids containing silver and gold nanoparticles were simulated, using water and ethylene glycol as the base fluid. The simulations were carried out using a modelled rectangular test cell, employing constant heat flux conditions through the ANSYS Fluent software. This study builds upon prior research by extending the comprehension of how nanofluids, particularly those involving silver and gold nanoparticles, can enhance photothermal absorption rates. The primary objective of this paper is to conduct a comparative analysis of the photothermal absorption rates exhibited by the two nanofluids under two simulation cases: (1) a constant heat flux applied to only one side of the wall and (2) a constant heat flux applied to both sides of the wall. The results show that both silver and gold nanofluids have excellent photothermal absorption rate and increase significantly when heat flux is applied to both sides of the wall. A better performance is observed for silver ethylene glycol-based nanofluid. Therefore, for a more photothermal absorption rate, it is recommended that silver ethylene glycol based nanofluid should be used.

Index-words: *Nanofluids, thermal absorption, solar collectors, photothermal absorption, gold nanofluid, silver nanofluid*

I. INTRODUCTION

Solar energy is a prominent renewable energy source that offers minimal environmental impact and has gained significant attention due to the increasing population and high electricity demand. It serves as a promising integral energy source, reducing greenhouse gas emissions and diversifying the energy supply [1]. With an annual solar energy production of 1.74 x 10^{17} W, it has the potential to meet global energy demands [2].

Solar energy can be captured through various methods, including photocatalytic, photoelectric, and photothermal conversion techniques [3]. In the realm of photothermal conversion, solar thermal collectors play a vital role in transforming solar energy into thermal energy, which can then be utilized for various applications. These collectors are broadly classified as concentrating and non-concentrating solar collectors, and further categorized as low, medium, and high temperature collectors [4].

To enhance the efficiency of solar thermal collectors, novel approaches have been explored, and nanofluids have emerged as a promising avenue. Nanofluids, which consist of nanoparticles suspended in a base fluid, have been extensively studied for their ability to improve heat transfer in applications such as solar collectors, heat exchangers, and radiators [5], [6]. Nanofluids utilize nanoparticles with sizes less than 100 nm, offering better heat conduction than conventional fluids due to their molecular-level interaction with the base fluid [7].

The application of nanofluids in solar thermal collectors aims to achieve enhanced thermal properties, including higher thermal diffusivity, thermal conductivity, and convective heat transfer coefficient [7]. These properties are influenced by factors such as nanoparticle volume fraction, size, shape, and the choice of base fluid.

Several advantages of nanofluids have been identified, including strong surface Plasmon resonance, high specific surface area enabling efficient heat transfer, and high photothermal conversion properties. However, they also face limitations such as sedimentation and aggregation in the fluid, as well as higher production and preparation costs [5].

In the context of solar thermal applications, silver and gold nanoparticles have been extensively studied for their thermal properties. Table I presents the thermal properties of silver and gold nanoparticles [8]. Furthermore, the choice of base fluid, such as water and ethylene glycol, also influences the thermal properties,

as shown in Table II [9].

TABLE I
THERMAL PROPERTIES OF SILVER AND GOLD NANOPARTICLE [8], [10]

Properties	Silver	Gold
Density (kg/m^3)	10500	19300
Specific Heat (J/Kg. K)	230	129
Thermal Conductivity (W/mK)	429	314

TABLE II
THERMAL PROPERTIES OF WATER AND ETHYLENE GLYCOL BASE FLUID [9], [11]

Properties	Water	Ethylene Glycol
Density (kg/m^3)	997	863
Specific Heat (J/Kg. K)	4179	2048
Thermal Conductivity (W/mK)	0.613	0.1404

The simulation and experimental analysis of nanofluids within solar thermal collectors require suitable test cells. Acrylic glass, a transparent thermoplastic homopolymer, has been commonly used due to its impact resistance and optical clarity. It serves as a versatile and cost-effective alternative to traditional glass, making it ideal for experimental observations.

In this study, the efficiency of silver and gold nanoparticles as direct sunlight absorbers in solar thermal applications was investigated using water and ethylene glycol as base fluids. The performance of these nanofluids was simulated for both one-sided and double-sided heat flux cases to account for solar tracking. Additionally, a comparison between gold and silver nanoparticles and their respective base fluids was conducted. This paper seeks to:

1. Investigate the photo-thermal absorption rate of nanofluids: (a) Gold-water, (b) Gold-ethylene glycol, (c) silver-water, (D) silver-ethylene glycol, for both cases were heat flux is applied to one side of the wall and heat flux applied to both sides of the wall.

2. Compare the photothermal absorption rate of gold and silver nanofluids.

This study makes a substantial contribution to the ongoing progression of solar energy technology, demonstrating the critical influence of nanofluid selection on photothermal absorption rates.

II. LITERATURE REVIEW

Enhancing the performance of solar energy systems has been the subject of extensive research. One approach that has gained significant attention is the use of nanofluids as heat transfer fluids in solar collectors. Several studies have investigated the benefits of nanofluids in improving the efficiency of solar energy harvesting devices.

The study by Tyagi et al. [12] revealed that Direct Absorption Solar Collectors (DASCs) using nanofluids as the working fluid exhibited up to 10% higher efficiency compared to flat-plate collectors. The presence of nanoparticles (NPs) in the nanofluids increased solar energy absorption by more than nine times compared to pure water.

Concurrently, the study conducted by Chaji et al. [13] delved into the efficiency impact of TiO2 nanoparticles, revealing efficiency enhancements of up to 15.7% with increased mass flow rates and up to 7% with TiO_2 particle additions.

Moreover, the thoughtful selection of nanofluids has emerged as a pivotal determinant in realizing performance increases within DASCs. For instance, Karami et al. [14] innovatively introduced carbon nanotube/water nanofluid into low-temperature DASCs, unveiling heightened photothermal conversion characteristics. Alongside, Meijie Chen et al. [15] conducted an exhaustive inquiry into the collector efficiency of silver nanofluids within direct absorption solar collectors, thus substantiating their prowess, particularly under real outdoor conditions.

Another valuable study by Ahmet Z. Sahin et al. [16] reiterated the efficiency gains achieved through nanofluid implementation. Their experiment yielded a notable 23.83% increase in solar collector efficiency compared to water. Intriguingly, they identified an optimum nanoparticle concentration, indicating the nonlinear nature of thermal conductivity's incremental trend.

A notable experimental investigation by Sanjay Kumar et al. [17] examined a direct absorption solar collector utilizing ultra-stable gold plasmonic nanofluid under real outdoor conditions. The outcomes of this study unveiled a remarkable enhancement in photothermal conversion efficiency, even at low particle loadings when gold nanoparticles (Au-NPs) were incorporated into water.

Parallel, Abdulhammed K. Hamzat et al. [18] conducted a comprehensive review that underscored the significance of nanofluid parameters on system performance. Their investigation indicated a 6.6% efficiency improvement

in a solar thermal system with CuO/water nanofluid compared to other conventional fluids. This aligns with related work by Menbari et al. [19], which demonstrated performance improvements in PTSC with CuO/water nanofluid and attributed the enhancement to nanofluid flow rate and nanoparticle volume fraction.

Similarly, the review by Panduro et al. [20] focused on the use of nanofluids as heat-transfer fluids in parabolic-trough collectors. It confirmed the well-established enhancement of thermal conductivity in nanofluids compared to base fluids. Various studies have investigated the dependence of thermal conductivity on nanofluid concentration and particle size.

TABLE III
SUMMERY OF RECENT RELATED WORKS

Study	Key Findings
Tyagi et al. [12]	DASCs with nanofluids up to 10% more efficient than flat-plate collectors. Significant increase in solar energy absorption with NPs.
Chaji et al. [13]	TiO_2 nanoparticles led to efficiency increases of up to 15.7% with increased mass flow rates and up to 7% with particle additions.
Meijie Chen et al. [15]	Real outdoor conditions demonstrated efficiency enhancement of silver nanofluids in direct absorption solar collectors.
Ahmet Z. Sahin et al. [16]	Experimental efficiency gain of 23.83% with nanofluid; identification of an optimum nanoparticle concentration.
Sanjay Kumar et al. [17]	Ultra-stable gold plasmonic nanofluids showcased remarkable photothermal conversion efficiency even at low concentrations.
Abdulhammed K. Hamzat et al. [18]	Nanofluids' impact on efficiency across diverse solar energy applications; emphasis on optimizing parameters.

In conclusion, these reviewed studies collectively highlight the immense potential of nanofluids in enhancing the performance of solar energy harvesting devices. Nanofluids have demonstrated superior thermal conductivity, heightened solar energy absorption rates, and improved collector efficiency in contrast to conventional fluids. However, further research endeavors are warranted to fine-tune parameters such as nanoparticle concentration, volume fraction, and flow rates for the attainment of peak performance. The application of nanofluids in solar energy systems holds promise in addressing energy demands and mitigating energy crises.

III. METHODOLOGY

A. System Parameter

In this section, the governing equations and models are briefly explained.

1. Transient flow

The simulation accounts for the transient nature of flow using the transient model in ANSYS. The solver solves each time step, eventually reaching a finite time step. Transient flows can be categorized into two types: forced transient and naturally occurring transients.

- Forced Transient: Time-dependent boundary conditions and source terms drive the transient flow field. Examples include rotor-stator interactions in a turbine or pulsing flow in a nozzle.
- Naturally Occurring Transients: Transient flow occurs due to the growth of instabilities within the fluid or a non-equilibrium initial fluid state. Examples include shock waves, heat absorption, and natural convection.

2. Governing equations

These equations mathematically describe the behavior of fluids, allowing engineers and scientists to analyze and predict fluid flow patterns, velocities, pressures, and other important properties. The governing equations are derived from fundamental principles such as conservation of mass, momentum, and energy. There are three primary equations commonly used: the continuity equation, the Navier-Stokes equations, and the energy equation. The equations stem from the fundamental principles of Newton's Laws and Reynolds transport theorem.

Mass conservation equation:

Continuity equation can be written in its general form using Gauss' divergence theorem by B. Sultanian., [21] and Emanuel, G., [22] as:

$$\frac{\partial \rho}{\partial t} + \nabla.(\rho V) = Sm. \quad (1)$$

This equation is applicable to both compressible and incompressible flows. The source Sm is the mass added continuous phase from a second phase and other user defined sources. For 2D axisymmetric geometry, the mass conservation equation can be given as Emanuel, G., [22]:

http://dx.doi.org/10.21622/RESD.2023.09.2.032

$$\frac{\partial \rho}{\partial t} + \frac{\partial}{\partial x}(\rho v \mathrm{X}) + \frac{\partial}{\partial r}(\rho v \mathrm{r}) + \frac{\rho v r}{r} = \mathrm{Sm}. \quad (2)$$

Momentum Equation

The Navier-Stokes equations, derived from Newton's second law of motion, describe the conservation of momentum in a fluid. The momentum equation in an inertial reference frame is given as:

$$\frac{\partial}{\partial t}(\rho . v) + \nabla . (\rho \vec{v} \vec{v}) = -\nabla P + \nabla . (\bar{\bar{T}}) + \rho \vec{g} + \vec{F}. \quad (3)$$

Were p being the static pressure, is the stress tensor, and are the gravitational force and external body forces.

The stress tensor is given by:

$$\bar{\bar{T}} = \mu[(\nabla \vec{v} + \nabla \vec{v} \mathrm{T}) - \frac{2}{3} \nabla . \vec{v} I] \quad (4)$$

Where μ is the molecular viscosity, I is the unit tensor and the second term on the right-hand side is the effect of volume dilation. Special practices related to the discretization of the momentum and continuity equation and their solution by means of the pressure-based solver are addressed in Ansys, 2009)

3. Multi-phase flow

Real-life flows often involve multiple phases. In multi-phase flow, a phase is defined as an identifiable class of material that has a particular inertial response to and interaction with the flow and potential field. The simulation considers multiple phases, such as liquid, gas, and solid (Ansys, 2012)

4. Volume of fraction (VOF)

The Volume of Fraction (VOF) model is a surface-tracking technique applied to a fixed Eulerian mesh. It is used for two or more immiscible fluids where the position of the interface between the fluids is of interest. The VOF model shares a single set of momentum equations for the fluids and tracks the volume fraction of each fluid in each computational cell throughout the domain (Ansys, 2010).

5. Modelling of nanofluid properties

It is important to determine the properties of nanofluid when solving the conservation equations. The needed properties include specific heat capacity, thermal conductivity, density, and dynamic viscosity. Using the following equations, the properties of gold and silver nanofluid were accounted for.

$$\rho_{nf} = \emptyset \rho_{np} + (1 - \emptyset) \rho_{bf} \quad (5)$$

The density of nanofluids is based on the mixture rule by Liu et al [23]

$$\mu \mathrm{nf} = (1 + 2.5\emptyset) \mu \mathrm{bf} \quad (6)$$

The viscosity is calculated considering the Brownian motion used by Batchelor et al. [24]

$$c_{\mathrm{p\,nf}} = \emptyset c_{\mathrm{pnf}} + (1 - \emptyset) c_{\mathrm{p\,bf}} \quad (7)$$

This specific heat is calculated based on the theoretical model by Gupta et al. [25]

$$k_{\mathrm{nf}} = \mathrm{k_{bf}} + ([1 + \frac{3(k_{np} - k_{bf})\emptyset}{k_{nf} + 2k_{bf} - (k_{np} - k_{bf})\emptyset}) \quad (8)$$

This thermal conductivity of nanofluid is calculated using the theoretical model of Xuan et al. [26]

B. Geometry and Mesh

Using Ansys® Space claim a 2D geometry that represented the setup was designed, with all the necessary constraints needed for solving a boundary value problem.

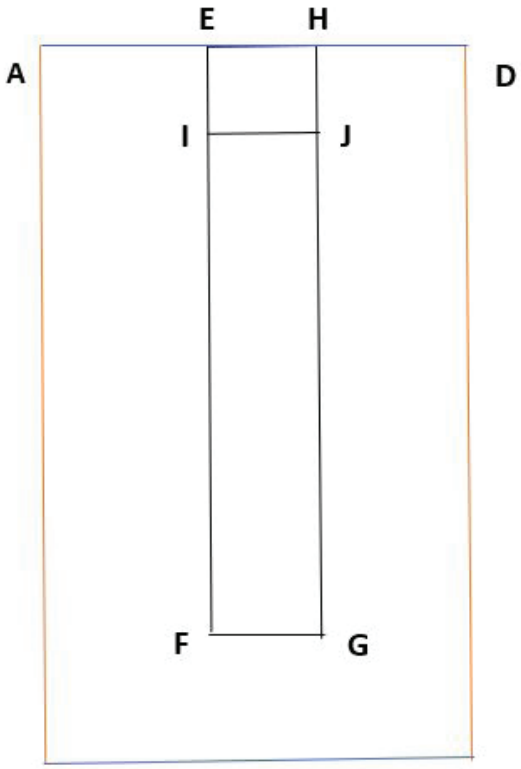

Fig. 1. Geometry

The walls AB and DC are exposed to sunlight (Heat flux is applied). While the wall EH is the pressure outlet, the remaining walls are all adiabatic. The geometry is then meshed to break the larger domain into pieces, which represents elements that can be designed in terms of the physical shape of the domain.

Volume 9, Issue 2, December 2023 - ISSN 2356-8569
http://dx.doi.org/10.21622/RESD.2023.09.2.032

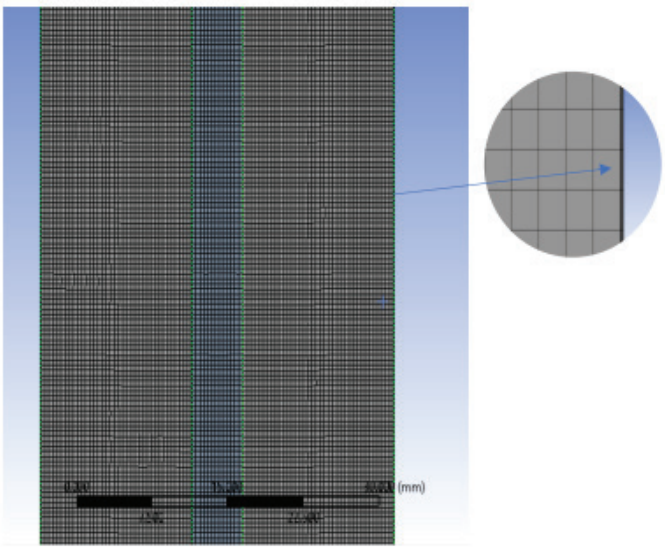

Fig.2. Mesh and inflation layers

Meshing is done to help reduce computational time and improve accuracy. During the meshing process five inflation layers were placed in the walls that have heat flux applied to them and the walls of the nanofluid region, to help capture the temperature profiles correctly near the no slip walls. A grid independence test was performed to find the optimal gird size for the simulation.

C. Simulation Setup

The simulation is carried out in Ansys® Fluent where the following parameters were setup.

TABLE IV
SIMULATION PARAMETERS

Solver	Pressure Based
Time	Transient
Total Time	7200 seconds
Step time	1
Materials	Nanofluid/Acrylic glass
Phase	Multi-phase
Scheme	Piso
Gradient	Least Square Cell Based
Formulation	Second Order Implicit
Initialization	Hybrid

The simulation was done in two cases where the heat flux is applied to just one side of the wall and the other case where the heat flux is applied to both sides of the walls. The Heat flux was calculated based on the geo-location with the help of the NASA and Solar Energy Database. To take into account the temperature profiles, surface monitors were placed on different points of the surface. This would help capture the temperature at different time steps as the simulation goes on.

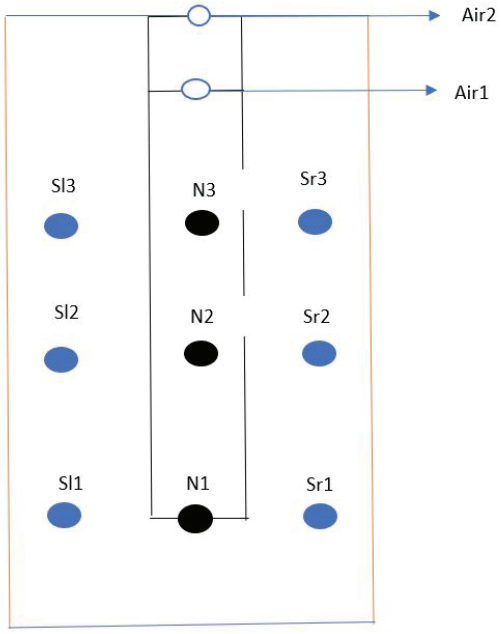

Fig.3. Surface monitors at different positions

Six surface monitors are placed in the acrylic glass region, three in the nanofluid region and two in the air region. The simulation focused on the Sl2, Sr2 and N2 surface monitors.

IV. Simulation Results

One of the difficulties faced in the simulation was how to factor in solar tracking. Since the simulation was 2D, the solar loading model could not be used, rather two cases were simulated, the first case is where the heat flux was applied to only one side of the wall to represent the solar irradiation at that side only, and the second case was simulated with the heat flux applied to both sides of the wall. Pressure was also neglected since the simulation involved a stationary nanofluid with no significant fluid motion. This analysis focuses on a two-hour period, a choice necessitated by constraints in computational resources, comparing different types of nanoparticles and base fluids under similar conditions. Temperature profiles for the simulation in the first case, where heat flux is only applied to the left side of the wall, are shown in Figures 4, 5, 6, and 7. The initial temperature for the simulation was 298.15 K.

Volume 9, Issue 2, December 2023 - ISSN 2356-8569
http://dx.doi.org/10.21622/RESD.2023.09.2.032

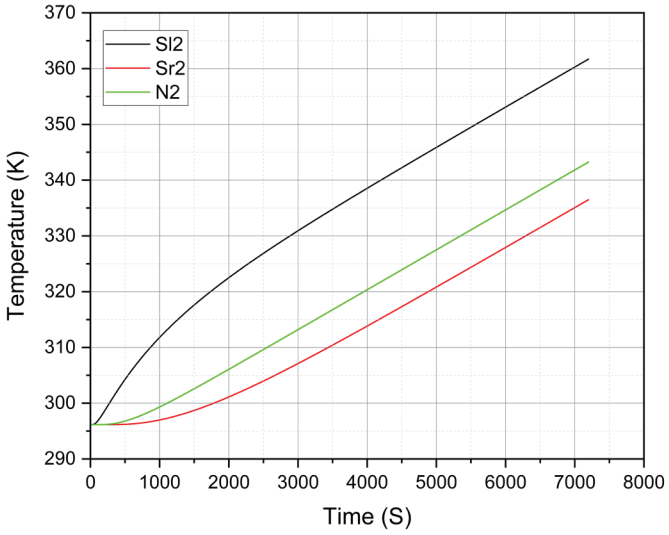

Fig.4. Temperature profile of Ag water-based nanofluid

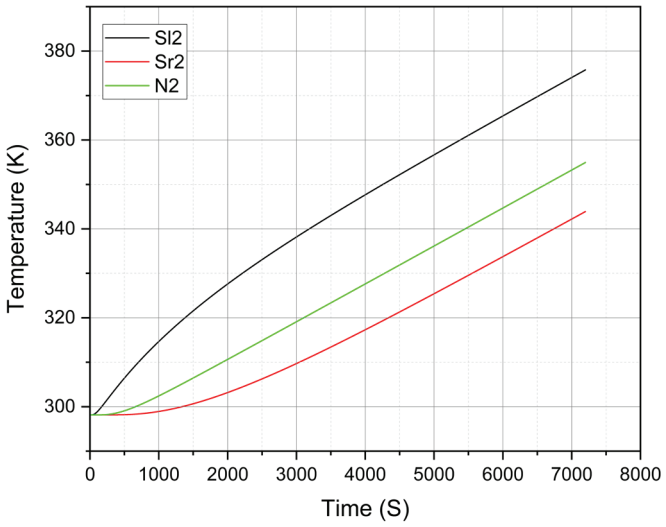

Fig.5. Temperature profile of Ag ethylene glycol-based nanofluid

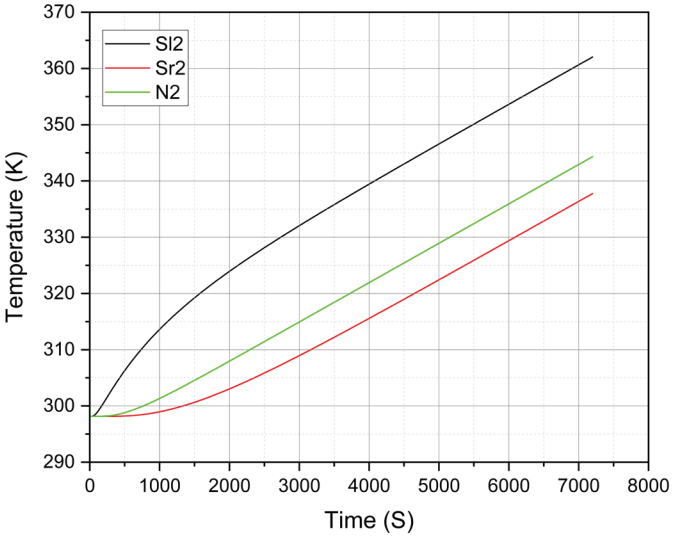

Fig.6. Temperature profile of Au water-based nanofluid

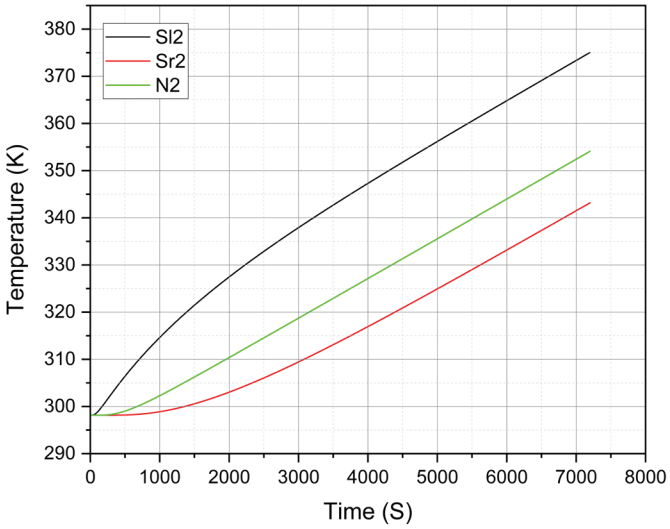

Fig.7. Temperature profile of Au ethylene glycol-based nanofluid

In the first case, where heat flux was applied to only one side of the wall, several intriguing observations were made. The temperature profiles revealed distinct temperature variations across different regions. The side of the wall with the heat flux (Sl2) exhibited the highest temperature, followed by the nanofluid region (N2), while the other wall without heat flux had the lowest temperature. These results highlight the impact of localized heat application and the subsequent thermal distribution within the system. However, it is important to note that the temperature variations were not uniform and were influenced by the specific nanoparticle and base fluid combinations used in the simulations. Analyzing the temperature profiles for different nanofluids, showed remarkable differences based on the choice of base fluid. For instance, in Figure 4, the temperature within the nanofluid region (N2) increased from an initial 298.15 K to 343.3 K, while the temperature within the left acrylic wall (Sl2) rose from 298.15 K to 361.7 K. In Figure 5, a similar trend is observed, with the temperature of the N2 region increasing from 298.15 K to 354.95 K and Sl2 reaching 375.78 K. These findings indicate a notable temperature increase of 19% and 26% in the nanofluid (N2) and left acrylic wall region (Sl2), respectively, when using an ethylene glycol base fluid. For water as the base fluid, the temperature increased by 15% in N2 and 21% in Sl2.

Figures 6 and 7 show a similar temperature pattern, with the N2 region reaching 344.33 K and 354.1 K, respectively, while Sl2 reached 362.05 K and 375.05 K. Using a water base fluid with gold nanoparticles (Au), a temperature increase of 15.5% in N2 and 21.4% in Sl2 was recorded. When employing ethylene glycol as the base fluid, the temperature increased by 18.8% in N2 and 25.8% in Sl2 respectively.

In the second case of the simulation, heat flux was applied to both sides of the wall. The temperature profile for the second case is shown in Figures 8, 9, 10 and 11.

Volume 9, Issue 2, December 2023 - ISSN 2356-8569
http://dx.doi.org/10.21622/RESD.2023.09.2.032

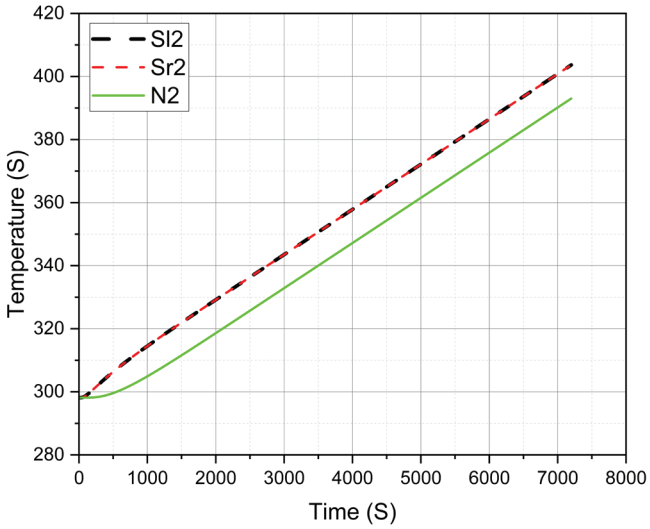

Fig. 8. Temperature profile of Ag water-based nanofluid

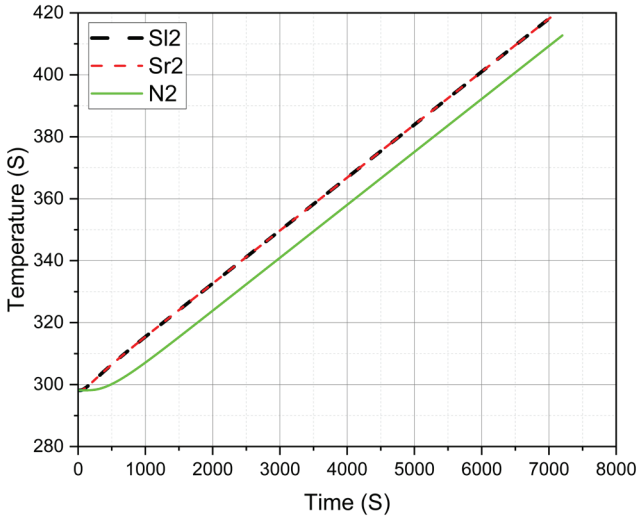

Fig. 9. Temperature profile of Ag ethylene glycol-based nanofluid

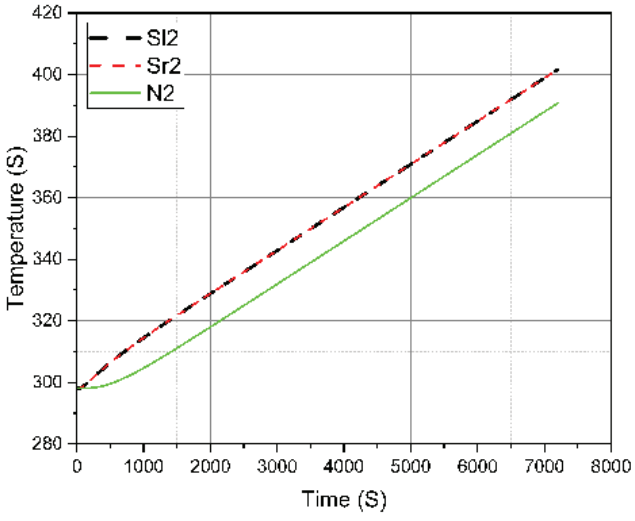

Fig.10. Temperature profile of Au water-based nanofluid

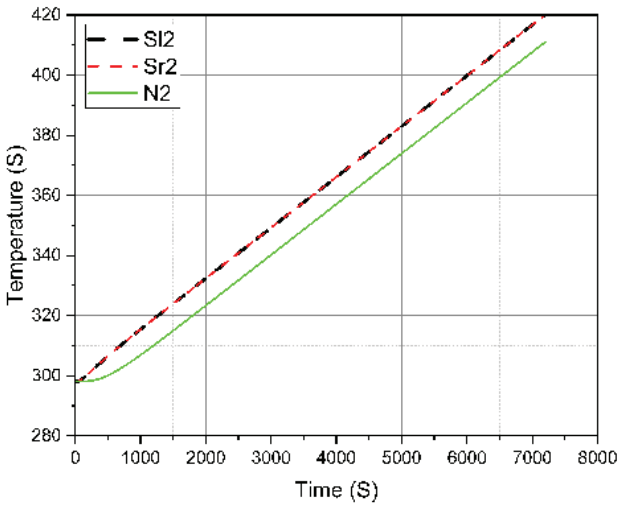

Fig.11. Temperature profile of Au ethylene glycol-based nanofluid

In a distinct set of experiments, the effects of uniform heat flux application to both the left acrylic wall region (Sl2) and the right acrylic wall region (Sr2) were examined. Consequently, Sl2 and Sr2 exhibited similar temperature profiles due to the uniform distribution of heat flux on both sides of the wall.

However, it is crucial to highlight that these temperature variations were non-uniform within the nanofluids themselves, as evident in Figures 8 and 9. In Figure 8, the temperature within the Nanofluid region (N2) increased substantially from 298.15 K to 393.04 K, while both Sl2 and Sr2 regions experienced an increase from 298.15 K to 403.67 K. Figure 9 followed a similar pattern, with the temperature profile of N2 rising from 298.15 K to 412.74 K and Sl2 and Sr2 temperatures rising from 298.15 K to 421.54 K.

These experiments utilized silver nanoparticles (Ag) within the nanofluid, with the choice of base fluid once again serving as the distinguishing factor. When employing water as the base fluid, the observed temperature gains were 31.83% in the nanofluid region (N2) and 35.39% in both acrylic wall regions (Sl2 and Sr2). Conversely, when ethylene glycol was employed as the base fluid, the recorded temperature enhancements were 38.43% in N2 and 41.39% in the acrylic wall regions (Sl2 and Sr2), respectively.

Finally, a consistent trend was observed in Figures 10 and 11, affirming the influence of base fluid choice on temperature profiles. In Figure 10, the temperature within N2 increased by 31.05%, and within Sl2 and Sr2, there was a temperature increase of 34.72%, all while using water as the base fluid. In Figure 11, employing ethylene glycol as the base fluid, a similar pattern emerged, with a 37.86% temperature increase in N2 and a 40.9% temperature increase in both acrylic wall

Volume 9, Issue 2, December 2023 - ISSN 2356-8569
http://dx.doi.org/10.21622/RESD.2023.09.2.032

regions (Sl2 and Sr2).

These extensive experiments underline the importance of base fluid selection within nanofluid systems, which can significantly impact temperature profiles and, consequently, the overall performance of heat transfer applications.

V. DISCUSSION

These findings demonstrate the significant influence of the base fluid on heat transfer characteristics and emphasize the importance of considering the thermophysical properties of the fluid when designing heat transfer systems. Tyagi et al. [12] highlight the importance of selecting the right nanofluid in improving the efficiency of solar energy harvesting devices. The results obtained from this simulation suggests that using ethylene glycol as a based fluid would provide higher thermal absorption as compared to water.

Similar trends were observed for gold nanofluids, indicating that the choice of base fluid remains a crucial factor in determining the system's thermal behavior. The temperature variations across different regions were consistent with those observed in the silver nanofluid simulations. These results suggest that the enhanced thermal performance attributed to nanoparticles is further influenced by the specific properties of the base fluid.

In the second case, where heat flux was applied to both sides of the wall, an entirely different temperature distribution pattern emerged. In this case, both sides of the wall experienced the highest temperatures. The equal application of heat flux on each side resulted in similar temperature rises, as expected. Comparing these results with those of the first case, it is evident that the temperature increases were more pronounced when heat flux was applied to both sides. This finding highlights the synergistic effect of dual-sided heat application, which leads to enhanced thermal characteristics within the system.

Upon examining the effects of different base fluids in the second case, it is observed that the choice of base fluid continued to play a pivotal role. When water was employed, silver nanofluid exhibited a 32% increase in temperature for N2 and a 35% increase for both walls (Sl2/Sr2). On the other hand, using ethylene glycol as the base fluid, the temperature increased by 38% in N2 and 41% in both walls. These results emphasize the significance of the base fluid in achieving optimal thermal performance and demonstrate the potential for further enhancing heat transfer efficiency in systems utilizing nanofluids. The results obtained are in line with Kumar et al. [17] investigation on ultra-stable gold plasmonic nanofluid. Both studies observed an increased efficiency of the working fluid. A comparison of the temperature changes in the nanofluids is presented in Table V.

TABLE V
TEMPRETURE AT NANOFLUID REGION (N2)

Cases		Nanofluid Region (N2) Temperature (K)			
	Nanoparticles	**Gold**		**Silver**	
	Base fluids	**water**	**ethylene glycol**	**water**	**ethylene glycol**
1	Initial	298.15	298.15	298.15	298.15
	Final	344.33	353.1	343.26	354.95
	Temperature (ΔT)	**15.49%**	**18.43%**	**15.13%**	**19.05%**
2	Initial	298.15	298.15	298.15	298.15
	Final	390.73	411.04	393.035	412.74
	Temperature (ΔT)	**31.05%**	**37.86%**	**31.83%**	**38.43%**

Comparing the performance of silver and gold nanofluids, it becomes evident that both types contribute significantly to an improved heat transfer coefficient, particularly when heat flux is applied to both walls. Furthermore, these findings highlight the superior thermal performance achieved by selecting ethylene glycol as the base fluid over water. This underscores the critical importance of meticulously considering the thermophysical properties of the base fluid during the design phase of heat transfer systems, an assertion made by Hamzat et al. [18] who similarly observed an increase in the thermal efficiency of solar thermal systems employing CuO/water nanofluids. These results are in alignment with the investigative experiment conducted by Filho et al. [27], which demonstrated a substantial increase in the thermal energy of silver nanofluids.

Additionally, comparing the silver ethylene glycol-based nanofluid with the gold ethylene glycol-based nanofluid, a 1% higher thermal absorption rate was observed in the silver nanofluid. While this difference may appear negligible in the short term, it holds importance for long-term simulations and should be considered when running simulations over extended periods.

This study introduces a critical factor that has been relatively less explored in previous research: the pivotal role of base fluid selection, especially when confronted with dual-sided heat application cases. The findings vividly illustrate how the choice of base fluid can exert substantial influence over temperature profiles and overall thermal performance. A remarkable temperature increases is observed achievable through the astute selection of base fluids, underscoring the potential for further optimization of heat transfer efficiency in nanofluid-based systems. In doing so, the study expands

the scope of knowledge in the field and contributes essential insights into the effective utilization of nanofluid for enhanced energy harvesting and heat transfer processes.

VI. CONCLUSION

The study investigated the effects of nanoparticle type and base fluid selection on the temperature profiles and heat transfer characteristics of nanofluids through a 2D simulation. Silver and Gold nanoparticles with water and ethylene glycol base fluids were investigated to study their photothermal absorption rate. The findings of this study underscore the critical role played by the choice of base fluid in nanofluid-based heat transfer systems. Notably, it was observed that the application of heat flux to both sides of the wall, as opposed to a single side, resulted in a significant increase in the photothermal absorption rate. This emphasizes the importance of solar tracking mechanisms to maximize photothermal efficiency, considering the dynamic positioning of the Earth relative to the sun. The results suggests that the use of ethylene glycol as base fluid in nanofluids should be used more often rather than water. The use of gold and silver nanofluid are promising since they both are good plasmonic materials and have good thermal conductivity but the enhancement of photothermal absorption is better found in silver nanofluid using ethylene glycol as its base fluid.

Nanofluids offer potential gains in energy efficiency, cost savings, and reduced greenhouse gas emissions, supporting sustainability. Enhanced thermal performance through nanofluids could lead to downsizing heat system components and wider adoption of renewable energy, fostering long-term economic benefits and energy security.

Further research is essential to comprehensively comprehend the complex dynamics and long-term performance of nanofluids in solar harvesting devices, encompassing considerations like nanoparticle stability, simulation time, system component effects, cost-effectiveness, and scalability.

VII. References

[1]C. Voyant *et al.*, "Machine learning methods for solar radiation forecasting: A review," *Renewable Energy*, vol. 105. 2017. doi: 10.1016/j.renene.2016.12.095.

[2] P. Kumari, and T. Durga, "Deep learning models for solar irradiance forecasting: A comprehensive review." *Journal of Cleaner Production* 318 (2021): 128566.

[3] A. R. Mallah, M. N. Mohd Zubir, O. A. Alawi, K. M. Salim Newaz, and A. B. Mohamad Badry, "Plasmonic nanofluids for high photothermal conversion efficiency in direct absorption solar collectors: Fundamentals and applications," *Solar Energy Materials and Solar Cells*, vol. 201, 2019, doi: 10.1016/j.solmat.2019.110084.

[4] J. Hanania, K. Stenhouse., Brodie Yyelland, J Donev. Solar Collector. 2018; Available from: https://energyeducation.ca/encyclopedia/Solar_collector.

[5] K. Farhana *et al.*, "Improvement in the performance of solar collectors with nanofluids — A state-of-the-art review," *Nano-Structures and Nano-Objects*, vol. 18. 2019. doi: 10.1016/j.nanoso.2019.100276.

[6] I. H. Yılmaz and A. Mwesigye, "Modeling, simulation and performance analysis of parabolic trough solar collectors: A comprehensive review," *Applied Energy*, vol. 225. 2018. doi: 10.1016/j.apenergy.2018.05.014.

[7] Ahmed, Mahmoud Salem. "Nanofluid: new fluids by nanotechnology." In *Thermophysical properties of Complex materials*. London, UK: IntechOpen, 2019.

[8] M. Nazeer, K. Ramesh, H. Farooq, and Q. Shahzad, "Impact of gold and silver nanoparticles in highly viscous flows with different body forces," *International Journal of Modelling and Simulation*, 2022, doi: 10.1080/02286203.2022.2084217.

[9] P. K. Pattnaik, J. R. Pattnaik, S. R. Mishra, and K. S. Nisar, "Variation of the shape of Fe3O4-nanoparticles on the heat transfer phenomenon with the inclusion of thermal radiation *Journal of Thermal Analysis and Calorimetry*, vol. 147, no. 3, 20218, doi: 10.1007/s10973-021-10605-9.

[10] S. Aghakhani, M. Afrand, A. Karimipour, R. Kalbasi, and M. Mehdi Razzaghi, "Numerical study of the cooling effect of a PVT on its thermal and electrical efficiency using a Cu tube of different diameters and lengths," *Sustainable Energy Technologies and Assessments*, vol. 52, 2022, doi: 10.1016/j.seta.2022.102044.

[11] H. F. Oztop, A. Z. Sahin, H. Coşanay, and I. H. Sahin, "Three-dimensional computational analysis of performance improvement in a novel designed solar photovoltaic/thermal system by using hybrid nanofluids," *Renew Energy*, vol. 210, 2023, doi: 10.1016/j.renene.2023.04.115.

[12] H. Tyagi, P. Phelan, and R. Prasher, "Predicted efficiency of a Low-temperature Nanofluid-based direct absorption solar collector," *Journal of Solar Energy Engineering, Transactions of the ASME*, vol. 131, no. 4, 2009, doi: 10.1115/1.3197562.

[13] H. Chaji, Y. Ajabshirchi, E. Esmaeilzadeh, S. Z. Heris, M. Hedayatizadeh, and M. Kahani, "Experimental study on thermal efficiency of flat plate solar collector using tio2/water nanofluid," *Mod Appl Sci*, vol. 7, no. 10, 2013, doi: 10.5539/mas.v7n10p60.

[14] M. Karami, M. A. Akhavan Bahabadi, S. Delfani,

and A. Ghozatloo, "A new application of carbon nanotubes nanofluid as working fluid of low-temperature direct absorption solar collector," *Solar Energy Materials and Solar Cells*, vol. 121, 2014, doi: 10.1016/j.solmat.2013.11.004.

[15] M. Chen, Y. He, J. Zhu, and D. Wen, "Investigating the collector efficiency of silver nanofluids based direct absorption solar collectors," *Appl Energy*, vol. 181, 2016, doi: 10.1016/j.apenergy.2016.08.054.

[16] A. Z. Sahin, M. A. Uddin, B. S. Yilbas, and A. Al-Sharafi, "Performance enhancement of solar energy systems using nanofluids: An updated review," *Renew Energy*, vol. 145, 2020, doi: 10.1016/j.renene.2019.06.108.

[17] S. Kumar, V. Sharma, M. R. Samantaray, and N. Chander, "Experimental investigation of a direct absorption solar collector using ultra stable gold plasmonic nanofluid under real outdoor conditions," *Renew Energy*, vol. 162, 2020, doi: 10.1016/j.renene.2020.10.017.

[18] A. K. Hamzat, M. I. Omisanya, A. Z. Sahin, O. Ropo Oyetunji, and N. Abolade Olaitan, "Application of nanofluid in solar energy harvesting devices: A comprehensive review," *Energy Conversion and Management*, vol. 266. 2022. doi: 10.1016/j.enconman.2022.115790.

[19] A. Menbari, A. A. Alemrajabi, A. Rezaei, "Heat transfer analysis and the effect of CuO/Water nanofluid on direct absorption concentrating solar collector", Applied Thermal Engineering, Volume 104, 2016, doi: 10.1016/j.applthermaleng.2016.05.064.

[20] E. A. Chavez Panduro, F. Finotti, G. Largiller, and K. Y. Lervåg, "A review of the use of nanofluids as heat-transfer fluids in parabolic-trough collectors," *Applied Thermal Engineering*, vol. 211. 2022. doi: 10.1016/j.applthermaleng.2022.118346.

[21] Sultanian, B. (2015). Fluid Mechanics: An Intermediate Approach (1st ed.). CRC Press. https://doi.org/10.1201/b18762

[22] Emanuel, G. (2016). Analytical Fluid Dynamics (3rd ed.). CRC Press. https://doi.org/10.1201/9781315148076

[23] J. Liu *et al.*, "Fullerene pipes," *Science (1979)*, vol. 280, no. 5367, 1998, doi: 10.1126/science.280.5367.1253.

[24] G. K. Batchelor, "The effect of Brownian motion on the bulk stress in a suspension of spherical particles," *J Fluid Mech*, vol. 83, no. 1, 1977, doi: 10.1017/S0022112077001062.

[25] H. K. Gupta, G. Das Agrawal, and J. Mathur, "An experimental investigation of a low temperature Al2O3-H2O nanofluid based direct absorption solar collector," *Solar Energy*, vol. 118, 2015, doi: 10.1016/j.solener.2015.04.041.

[26] Y. Xuan, Q. Li, W. Hu, Aggregation structure and thermal conductivity of nanofluids, AIChE J. 49 (2003)

[27] E. P. B. Filho, O. S. H. Mendoza, C. L. L. Beicker, A. Menezes and D. Wen, "Experimental investigation of a silver nanoparticle-based direct absorption solar thermal system." *Energy conversion and Management* 84 (2014): 261-267, ISSN 0196-8904.

Journal of Renewable Energy and Sustainable Development (RESD) Volume 9, Issue 2, December 2023 - ISSN 2356-8569
http://dx.doi.org/10.21622/RESD.2023.09.2.042

Received on, 09 September 2023 Accepted on, 29 November 2023 Published on, 20 December 2023

Computational Simulation Study of the Impact of Isotropic GDL Thermal Conductivity on PEMFC Characteristics

Mahmut Kaplan

Department of Machine and Metal Technology, Naci Topcuoglu Vocational High School, Gaziantep University, Gaziantep, Turkey

mahmutkaplan@gantep.edu.tr

ABSTRACT

The technical capability of proton exchange membrane fuel cell (PEMFC) offers an encouraging solution to produce sustainable and clean power. The gas diffusion layer (GDL) is a pivotal part of the PEMFC which plays a critical role in providing a pathway for reactant and product. GDL electrically connects the catalyst layer to the current collector and conducts heat generated in the electrochemical reactions. The thermal conductivity is one of the most important transport properties of the GDL that affects heat transfer across the cell and the overall performance. In the current work, the impact of the isotropic GDL thermal conductivity ranging 1-100 W/mK at 0.4 and 0.6 V on the cell efficiency is studied computationally using ANSYS Fluent PEMFC module. The results indicate that an increase in the isotropic GDL thermal conductivity enhances the fuel cell current density considerably up to 20 W/mK with the more homogeneous temperature distribution and lower temperature across PEMFC at 0.4 and 0.6 V. After this, the impact of the GDL thermal conductivity on the performance diminishes and thus the current density is nearly constant with further increase in isotropic GDL thermal conductivity at both cell voltages. The peak current density of 1.37 A/cm2 is gained at 100 W/mK. The power function provided a good fit with the calculated data. Oxygen consumption and water production augments with higher thermal conductivity, especially the regions above the cathode current collector ribs.

Index-words: *PEMFC, GDL, Thermal conductivity, Heat transfer, Performance; CFD.*

I. INTRODUCTION

Internal combustion engines are widely applied to a power source for commercial and passenger vehicles over the past decades. They consume carbon-based fossil fuels (gas or diesel) which are the non-renewable energy sources producing significant pollutants such as greenhouse gasses (CO_2, CH_4, and N_2O), hazardous gases (CO, and NO_x) and particulate matter. Their extensive use leads to degrading the air quality, detrimental health problems and climate change. The largest chunk of greenhouse gas is owing to CO_2 production accounted for 76% of the emitted global greenhouse gases in 2010 (Towoju and Ishola, 2020). Therefore, in the last two decades, alternative power sources such as hydrogen energy systems have been improved to solve problems (Dincer, 2008; Barbir, 2013). A fuel cell as an electrochemical energy converter is one of the of the most encouraging alternative energy sources of the future. It produces quiet, efficient and clean electricity. Proton exchange membrane fuel cell (PEMFC) is the most distributed cell type owing to having low-temperature operation, modularity, light weight and being suited for a variety of applications including portable power, backup power and automotive applications (Spiegel, 2008). A PEMFC is a multi-component device containing a membrane-electrode assembly (MEA) and current collectors having flow channels machined. The MEA is comprised of anode and cathode catalyst layer (CL) and gas diffusion layer (GDL) being separated by a polymer membrane. The oxidation and reduction reactions occur inside the anode and cathode CL, respectively. Hydrogen is broken down into protons and electrons at the anode CL. Protons travel throughout the PEMFC whereas electrons move via an external circuit toward the cathode. They react with oxygen, and as a result the electricity, water and waste heat are produced at the cathode CL. GDLs being the outermost layers of the MEA serve to transport of water, electrons and heat generated in the cell reactions from CL to bipolar plates (Cindrellaa et al., 2009). Besides, GDL as a porous medium provides a pathway for reactants from the gas channel to CL and mechanical support to the MEA (Okonkwo and Otor, 2021). GDL properties such as porosity, diffusivity, permeability, electrical and thermal conductivity affect transport behaviour of PEMFC (Athanasaki et al., 2023). Thermal conductivity as a significant GDL transport property plays a dominant role in the temperature distribution of PEMFC and moving heat by the diffusion (Omrani and Shabani, 2019). The waste heat induced throughout the cathode reaction at the CL is a primary heat source affecting the temperature distribution of PEMFC. The heat can be taken away from the cell by conduction (solid structure) and convection (species flow).

Besides, the reactant gases and product water discharge the residual heat into the environment (Zamel and Li, 2013). In the bipolar plates connected electrodes by GDLs, the heat is dissipated by both conduction and convection owing to their embedded flow channels. Since the bipolar plates have higher thermal conductivity compared with that of the gases in the channels, heat can be easily taken away from the plates. That is, the heat transfer from the GDL region close to gas channels is lower than the region close to the lands. Therefore, GDL thermal conductivity strongly affects temperature distribution and heat removal capability of PEMFC. Turkmen et al. (2023) calculated the GDL thermal conductivity under various working temperatures (20-80 °C). It was concluded that high cell temperature had a positive impact on the thermal conductivity in the electrodes. They also suggested several correlations (polynomial, rational and power) to express the thermal conductivity depending on the temperature.

In literature (He et al., 2010; Alhazmi, 2013; Chowdhury et al., 2016; Alcántara, 2022) and a variety of computational and experimental investigations have been carried out to understand the influence of GDL thermal conductivity on PEMFC performance. He et al. (2010) improved a two-phase, three-dimension model to scrutinize the impact of the anisotropy of GDL thermal conductivity along the x, y and z directions on the water and heat management. The results demonstrated that compared to isotropic GDL, larger temperature difference was produced by the anisotropic GDL, especially the in-plane conductivity perpendicular to the gas channels, which led to the reduction in the current density and non-uniform water saturation compared to the isotropic case. Alhazmi et al. (2013) examined the effects of anisotropic GDL thermal conductivity on the performance at various operating temperatures for both through-plane (1-10 W/mK) and in-plane (1-100 W/mK) directions using the PEMFC module of ANSYS FLUENT. They found that a rise in the in-plane and through-plane thermal conductivity resulted in significantly higher power density of PEMFC. They also reported that the temperature gradients and maximum temperature in PEMFC decreased when increasing GDL thermal conductivity in both directions.

Alcántara et al. (2022) studied the influence of the distinct GDL transport features on the performance employing the CFD software ANSYS FLUENT and they reported that lower GDL thermal conductivity led to high temperatures and temperature gradients in the membrane. The temperature gradient is a key parameter that affects both heat and water transfer in PEMFC and thus the long-term stability and durability of the cell components (Ozden, 2019).

Based on the literature, it is concluded the GDL thermal conductivity influences the temperature difference in the PEMFC and thus the performance characteristics. Temperature distribution through GDL influences water and heat transport mechanisms, and hence the durability of PEMFC parts. The anisotropic GDL augments the temperature variation and results in more non-uniform current density compared to the isotropic GDL. There are a lot of studies related to the effect of anisotropic GDL on heat transfer and PEMFC performance. But there is not enough information available on the interactions between the isotropic GDL thermal conductivity, gas species concentrations and temperature distribution through the components.

The current work aims to study the influence of the isotropic thermal conductivity of the GDL on the temperature, oxygen and water distribution inside the porous layers and the cell performance. The findings of this research study can be beneficial to researchers, designers, and engineers for improving design and performance of the PEMFC system.

II. METHODS AND MATERIALS

A. CFD Model and Operating Parameters

In this computational study, the PEMFC geometry is adopted from Wang et al.'s (2003) experiment. The length and width of the fuel cell are 0.07 and 0.002 m, respectively. The electrolyte projected area is specified as 0.00014 m^2. The height and width of gas channels are 0.01 m. The CLs, GDLs, and membrane thicknesses are 1.29×10^{-5}, 3×10^{-4} and 1.08×10^{-4} m, respectively (Kaplan, 2022a).

Volume 9, Issue 2, December 2023 - ISSN 2356-8569
http://dx.doi.org/10.21622/RESD.2023.09.2.042

The operating characteristics of the model are provided in Table I. Thermal conductivity of the components is given in Table II.

TABLE I: OPERATING FEATURES OF PEMFC.

Parameter	Value
Temperature of the cell	343 K
Open circuit potential of the cell	0.94 V
Reference exchange current density (anode and cathode)	4000 and 0.1 A/m^2
Inlet mass flow rate (anode and cathode)	5.40 x 10^{-6} and 3.29 x 10^{-5} kg/s
Inlet H_2 and H_2O mass fraction (anode)	0.2 and 0.8 (Kaplan, 2022b)
Inlet O_2 and H_2O mass fraction (cathode)	0.2 and 0.1 (Kaplan, 2022b)
H_2O and H_2 reference diffusivity	7.33 x 10^{-5} m^2/s (Biyikoglu and Alpat, 2011)
O_2 and other species reference diffusivity	2.13 x 10^{-5} and 4.9 x 10^{-5}m^2/s
Porosity and viscous resistance GDL and CL	0.5 and 1 x 10^{12} 1/m^2 (Kahveci and Taymaz, 2018)
Surface/volume ratio of CL	200000 1/m
Anodic and cathodic transfer coefficient at anode and cathode	0.5 and 2 (Wang et al., 2003)

TABLE 2: THERMAL CONDUCTIVITY OF CELL COMPONENTS.

Components	Value
Bipolar plate	100 W/mK
GDL	1-100 W/mK
CL	10 W/mK
Membrane	2 W/mK

B. Assumptions

The assumptions employed in the current 3D PEMFC model are:

- The calculation process of PEMFC is under the steady state condition.
- The flow is laminar and incompressible.
- The gas species are supposed to be as perfect gases.
- The MEA are regarded as isotropic and homogenous porous medium.
- Contact resistance between different layers is neglected.
- Gas cross-over through the membran is ignored.

C. Conservation Equations

The following conservation equations govern physical phenomena occurring within a PEMFC:

$$\nabla(\rho\vec{u}) = 0 \quad (1)$$

$$\frac{1}{(\varepsilon)^2}\nabla(\rho\vec{u}\vec{u}) = -\nabla P + \nabla(\tau) + S_m \quad (2)$$

$$\nabla(\vec{u}C_i) = \nabla(D_i^{eff}\nabla C_i) + S_i \quad (3)$$

$$\nabla(\rho c_p \vec{u}T) = \nabla(k^{eff}\nabla T) + S_e \quad (4)$$

$$\nabla(\sigma_{mem}\nabla\phi_{mem}) + R_{mem} = 0,\ \nabla(\sigma_{sol}\nabla\phi_{sol}) + R_{sol} = 0 \quad (5)$$

$\vec{u}$ and ρ are the velocity vector and density of species. ε is the porosity of porous media. P and τ are the species pressure and viscous stress tensor. C_i and D_i^{eff} are the species (i) mass fraction and effective diffusion coefficient. c_p and k_{eff} the constant-pressure heat capacity and effective thermal conductivity. T is the temperature. R_{mem}, ϕ_{mem}, σ_{mem} and R_{sol}, ϕ_{sol}, σ_{sol} are the volumetric transfer current, electric potential and electrical conductivity of membrane and solid electrode, respectively. S_m, S_i and S_e are the source terms of the momentum, species and energy, respectively.

D. Boundary Conditions

On the inlet and outlet faces of the gas channels, the fixed mass flow rate and pressure boundary conditions are imposed, respectively. All other surfaces are the no-slip with zero flux wall boundary conditions. The surfaces of the current collectors are represented as the anode and cathode terminals on which their potentials are set to 0 V and 0.4-1 V, respectively, for drawing the polarization curve. The temperature of inlet fuel and air is 343 K.

E. Numerical Methodology

All parts of the geometry required to ANSYS Fluent Fuel Cell Module (ANSYS, 2013) are created and assembled using SOLIDWORKS software. The structured hexahedral mesh is generated for each component of

PEMFC using the sweep method in ANSYS Meshing in Figure 1. The modelling domain involves 1254400 cells obtained by the grid independence test in a previous study (Kaplan, 2021). The governing equations used in the present computations are solved with pressure-based solver algorithms based on finite volume method in CFD software ANSYS Fluent. The SIMPLE algorithm is chosen as a solver scheme. The Least Squares Cell Based discretization method is selected for the gradient. The Second Order discretization scheme is employed for pressure, momentum, density and species.

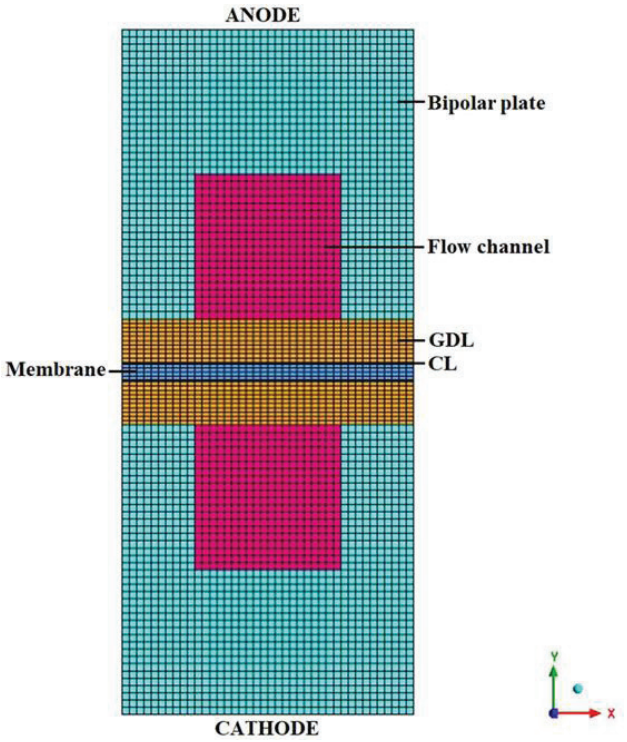

Fig 1. Meshed computational domain of PEMFC model

F. Model Validation

In the present work, the CFD model validation is conducted using the measured data (Wang et al., 2003) in Figure 2. It is seen that the polarization curve demonstrates good agreement with the measured data, particularly at low and medium current densities. The overprediction is seen at high current densities. The most probably reason for this is that the present model disregards the liquid water presence inside the porous layers leading to a decrease in porosity of the layers and a rise in species mass transfer resistance.

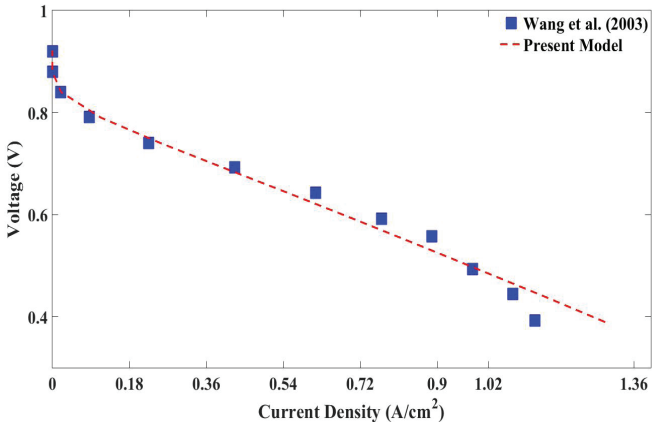

Fig 2. Polarisation curve for the numerical predictions compared with the measured data

III. RESULTS AND DISCUSSION

The present study focuses on examining the influence of the isotropic GDL thermal conductivity on the performance characteristics of PEMFC. Figure 3 indicates the cell current density versus GDL thermal conductivity (1-100 W/mK) plots at 0.4 and 0.6 V. The current density shows the same trend at both cell voltages in Figure 3: a rise with increasing the GDL thermal conductivity.

The influence of GDL thermal conductivity on PEMFC performance diminishes after 20 W/mK and the current density is almost constant with further increase in isotropic GDL thermal conductivity.

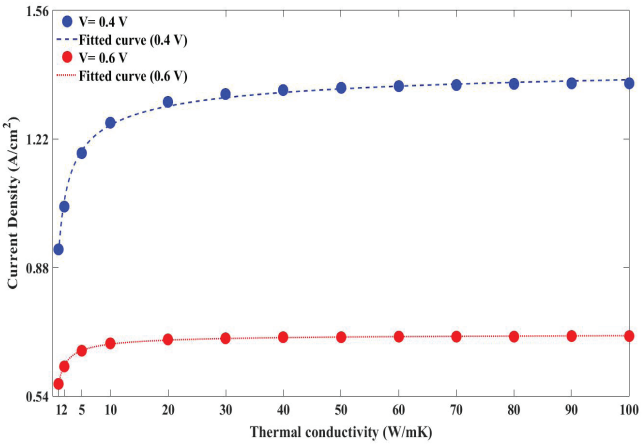

Fig 3. Current density versus GDL thermal conductivity plot at 0.4 and 0.6 V

Türkmen et al. (2023) experimentally examined the influence of temperature change on the GDL thermal conductivity and they reported that the power type correlation was the most suitable to describe thermal conductivity evaluated as a function of the measured temperature. Similar to Türkmen et al. (2023), the calculated data points are fitted to a power function of the form as:

Volume 9, Issue 2, December 2023 - ISSN 2356-8569
http://dx.doi.org/10.21622/RESD.2023.09.2.042

$$I = ak^b + c \quad (5)$$

where I is current density and k is the GDL thermal conductivity. a, b and c are coefficients in Equation (5) which are determined using the MATLAB Curve Fitting Toolbox. a = –0.5243, b = –0.452 and c = 1.442 at 0.4 V. a = –0.1345, b = –0.6798 and c = 0.7054 at 0.6 V. The R-square value of the power function at 0.4 and 0.6 V is 0.99 with a 95% confidence bound. Fitted curves for 0.4 and 0.6 V in Figure 3 are shown by dashed and dotted lines, respectively.

It is clear in Figure 3 that the maximum current density is achieved with the GDL thermal conductivity of 100 W/mK at 0.4 V. As is evident in Figure 3, an increase in the GDL thermal conductivity from 1-10 to 100 W/m K leads to an improvement of the current density of the PEMFC from 0.92-1.26 to 1.37 A/cm^2, respectively. In the following sections, the impact of different isotropic GDL thermal conductivities (1, 10 and 100 W/mK) on the distribution of temperature, oxygen and water in the PEMFC is examined at 0.4 V.

A. Influence of the GDL Thermal Conductivity on the Cell Temperature

Figure 4 illustrates the temperature distribution for two different cathode GDL regions: near the CL and near the flow channel (NCL and NFC) for thermal conductivities of 1, 10 and 100 W/mK at 0.4 V.

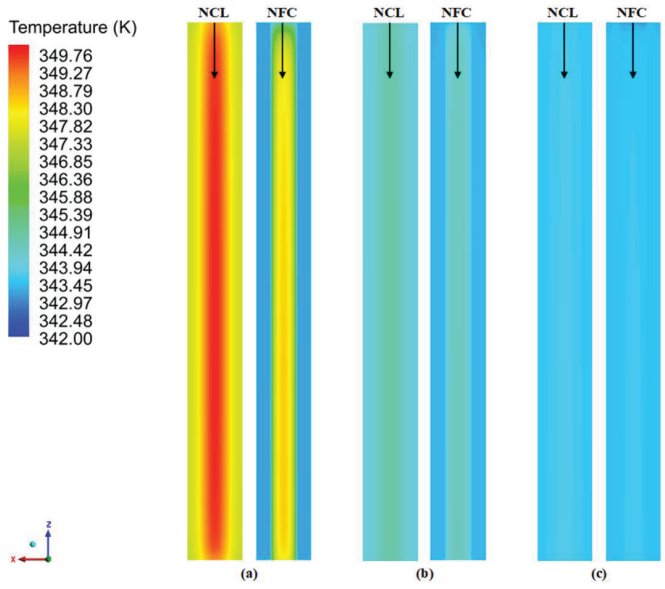

Fig 4. Influence of GDL thermal conductivity on temperature distribution in two regions close to CL and close to flow channel at (a) 1 W/mK, (b) 10 W/mK, and (c) 100 W/mK

It is seen in Figure 4 that an increase in the GDL thermal conductivity decreases temperature in two selected GDL regions. The sensitivity of the temperature gradient in the selected regions diminishes with higher GDL thermal conductivity. of PCM The maximum temperature of 349.76 K is observed near the CL region at 1 W/mK due to heat transfer rate being poor at low GDL thermal conductivity in Figure 4a.

Temperature decreases towards the flow channel at 1, 10 and 100 W/mK in Figure 4. Meanwhile, temperature above the land regions is lower than that above the flow channel, especially at 1 and 10 W/mK due to bipolar plate thermal conductivity being higher than that of the gas species. Besides, temperature homogeneity enhances remarkably with the GDL thermal conductivity of 100 W/mK in Figure 4c.

Figure 5 shows temperature distribution along to lateral direction at the inlet and outlet of the middle of cathode GDL thickness for various GDL thermal conductivities. An increase the GDL thermal conductivity results in decreasing temperature at the inlet and outlet in Figure 5.

Besides, temperature at the outlet is higher than the inlet temperature in Figure 5. However, temperature difference between inlet and outlet decreases with increasing thermal conductivity from 1 to 100 W/mK. It is found that temperature distribution over the mid-thickness of cathode GDL is more uniform at 100W/mK in Figure 5.

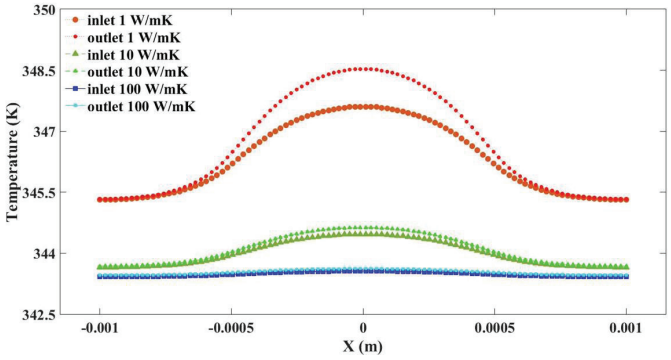

Fig 5. Comparison of lateral temperature distribution at the inlet and outlet of mid-thickness of GDL for different GDL thermal conductivities

Figure 6 shows temperature distribution at the middle of the cell length for GDL thermal conductivities of 1, 10 and 100 W/mK. As illustrated in Figure 6, temperature through the MEA is very high and non-uniform at 1 W/mK.

The elevated temperature in PEMFC leads to a dry membrane which reduces protonic conductivity through the cell and facilitates the membrane fracture. An increase in the GDL thermal conductivity from 1 to 100 W/mK leads to more homogeneous temperature distribution and lower temperature throughout PEMFC in Figure 6. It is concluded that augmenting GDL thermal conductivity results in a decrease in the temperature gradient and an enhancement in temperature homogeneity thoroughly the cell.

Volume 9, Issue 2, December 2023 - ISSN 2356-
http://dx.doi.org/10.21622/RESD.2023.09.2.042

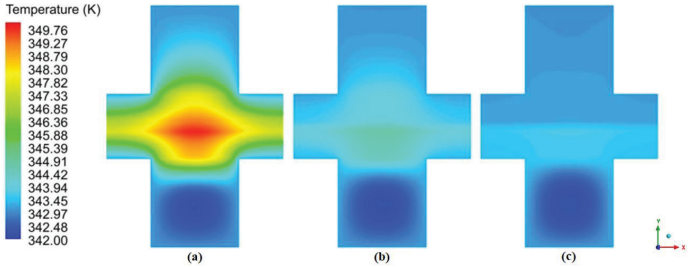

Fig 6. Comparison of temperature distribution at the middle of the cell length for three different GDL thermal conductivities: a) 1 W/mK, b) 10 W/mK, and c) 100 W/mK at 0.4 V

B. Influence of the GDL Thermal Conductivity On the Oxygen and Water Concentration

Figure 7 shows the oxygen concentration distributions of two cathode GDL regions: close to the CL and close to the channel for various thermal conductivities of 1, 10 and 100 W/mK at 0.4 V.

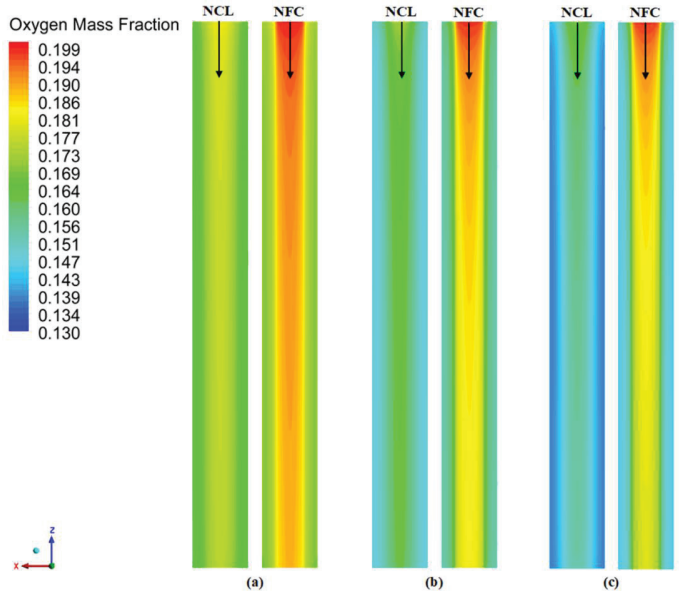

Fig 7. Influence of GDL thermal conductivity on oxygen distribution in two regions close to CL and close to flow channel at (a) 1 W/mK, (b) 10 W/mK, and (c) 100 W/mK

There is a significant correlation between enhanced current density obtained with higher GDL thermal conductivity and oxygen consumption in the GDL in Figure 7. The trend is clear that the oxygen mass fraction reduces significantly when the GDL thermal conductivity elevates from 1 to 100 W/mK for two regions. As illustrated in Figure 7c, the maximum oxygen consumption is obtained with a GDL thermal conductivity of 100 W/mK in the region near the cathode CL where the hydrogen/oxygen reaction occurs. Besides, the amount of oxygen in the region above the flow channel is higher than in the regions above the bipolar plate because of the rib regions not directly connected to the flow channels and suffering from a slow oxygen mass transfer. Figure 8 shows comparison of lateral oxygen distribution at the inlet and outlet of mid-thickness of GDL for various GDL thermal conductivities.

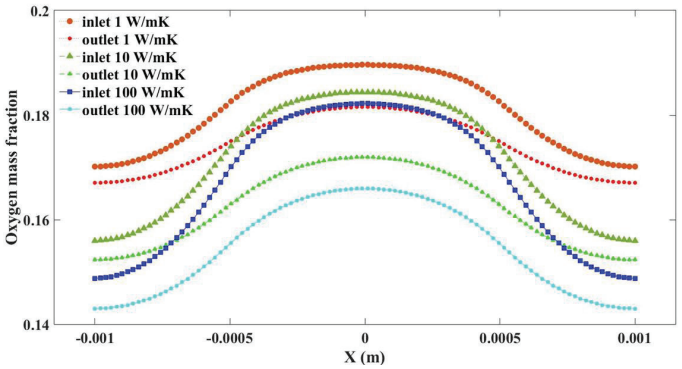

Fig 8. Comparison of lateral oxygen distribution at the inlet and outlet of mid-thickness of GDL for different GDL thermal conductivities

Oxygen mass fraction decreases from inlet to outlet owing to oxygen diffusion into the cathode CL in Figure 8. Besides, an increase in GDL thermal conductivity from 1 to 100 W/mK leads to lower oxygen concentration for two regions. Similar to Figure 7, the maximum oxygen mass fraction is detected in the region above the channel.

Figure 9 demonstrates oxygen concentration contour in the cathode channel, GDL and CL at a midway location between inlet and outlet. A strong decrease of oxygen in the cathode CL and GDL is observed as the thermal conductivity increases from 1 to 100 W/mK at 0.4 V in Figure 9. It is clear that the higher oxygen concentration is detected in the region above the channel whereas it is remarkably lower in the regions above the lands where they are not directly exposed to the channels in Figure 9.

Figure 10 demonstrates the water concentration distributions of two regions: close to CL and close to the channel for different thermal conductivities (1-100 W/mK) at 0.4 V. There is an opposite relation between water and oxygen mass fraction.

Unlike the oxygen mass fraction in Figure 7, the water mass fraction enhances remarkably when the GDL thermal conductivity increases from 1 to 100 W/mK in Figure 9. It is clear in Figure 10c that the maximum water production is achieved at 100 W/mK in the region near the cathode CL due to the electrochemical reaction.

An increase in water generation with higher GDL thermal conductivity results in more hydrated membrane and reduction of ohmic loss. Besides, the water concentration augments in the regions above the lands because of higher oxygen consumption there.

Volume 9, Issue 2, December 2023 - ISSN 2356-8569
http://dx.doi.org/10.21622/RESD.2023.09.2.042

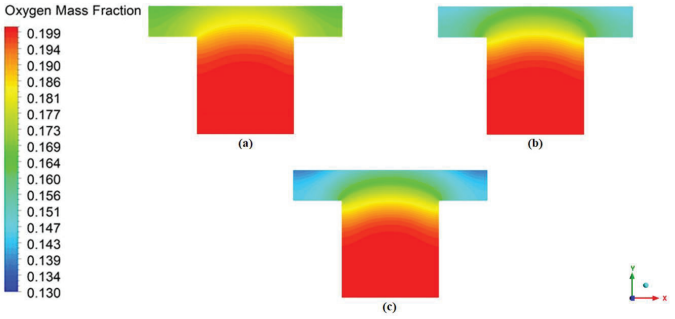

Fig 9. Oxygen distribution throughout cathode CL, GDL and flow channel for three different GDL thermal conductivities: a) 1 W/mK, b) 10 W/mK, and c) 100 W/mK at 0.4 V

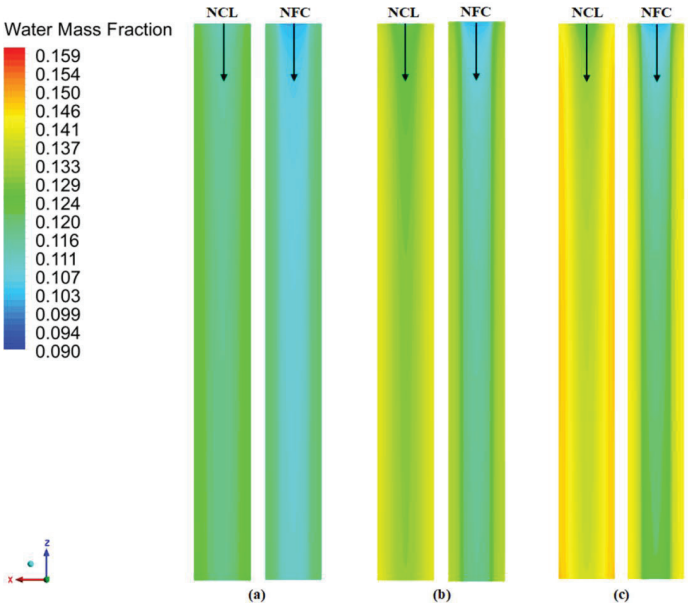

Fig 10. Influence of GDL thermal conductivity on water distribution in two regions close to CL and close to flow channel at (a) 1 W/mK, (b) 10 W/mK and (c) 100 W/mK

Figure 11 demonstrates comparison of water distribution at the inlet and outlet of mid-thickness of GDL for various thermal conductivities. The mass fraction of water increases gradually from inlet to outlet due to water produced by the cathode reaction in Figure 11.

Figure 12 indicates water concentration contour in the cathode channel, GDL and CL at a midway location between inlet and outlet. A strong increase of water mass fraction in the CL and GDL is observed as the thermal conductivity increases from 1 to 100 W/Mk in Figure 12. In addition, the water removal from the GDL is higher in the region above the gas channel compared with that in the regions above the ribs because of the channel allowing direct contact of water to the GDL.

The results show that higher GDL thermal conductivity leads to reducing oxygen concentration and augmenting water concentration in both the lateral and longitudinal directions.

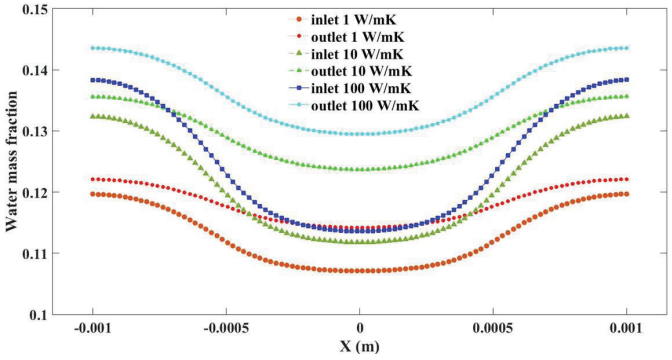

Fig 11. Comparison of lateral water distribution at the inlet and outlet of mid-thickness of GDL for different GDL thermal conductivities

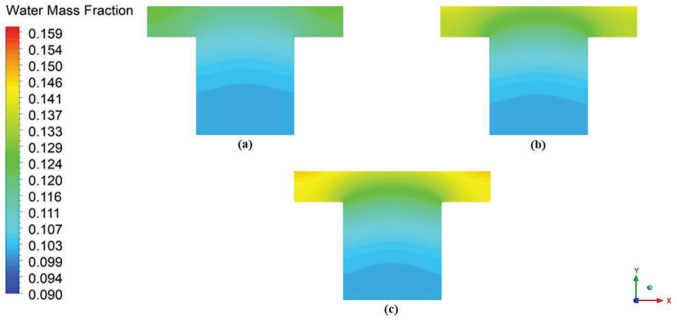

Fig 12. Water distribution throughout cathode CL, GDL and flow channel for three different GDL thermal conductivities: a) 1 W/mK, b) 10 W/mK, and c) 100 W/mK at 0.4 V

IV. CONCLUSIONS

In the current work, the impact of GDL thermal conductivity on PEMFC performance is scrutinized by CFD method. The results show that:

- The power function is a good fit to the calculated current density data obtained at 1-100 W/mK.
- Elevating isotropic GDL thermal conductivity results in temperature gradient reduction and more homogeneous temperature distribution in the cell.
- The water mass fraction intensifies in the regions above the ribs of the cathode current collector thanks to higher oxygen consumption there.
- The increased hydration with higher isotropic thermal conductivity improves the proton conductivity of the membrane and PEMFC performance.
- The PEMFC performance enhanced with higher thermal conductivity of GDL. But the impact of GDL thermal conductivity on PEMFC performance decreases after 20 W/mK and the current density is nearly fixed with further increase in isotropic GDL thermal conductivity at 0.4 and 0.6 V. This is due to increase in thermal conductivity from 1 to 20 W/mK leads to a reduction in temperature difference thanks to heat removal from the cell and thus almost uniform temperature distribution along the GDL.

These outcomes provide key insights for improving the design and performance of PEMFC, which are pivotal for the commercialisation of PEMFC technology and diverse applications including portable power and automotive applications.

V. References

[1] N. Zamel and X. Li, "Effective transport properties for polymer electrolyte membrane fuel cells e with a focus on the gas diffusion layer," *Prog Energy Combust Sci*, vol. 39, pp. 0–39, 2013.

[2] G. Wei, C. Wang, C. Jiang, and J. Zhang, "The Investigation of Flow Channel Design on the Performance of PEM Fuel Cell," *ECS Meeting Abstracts*, vol. MA2017-01, no. 22, 2017, doi: 10.1149/ma2017-01/22/1133.

[3] A. Can Turkmen, M. Espinoza-Andaluz, C. Celik, B. Sunden, and H. Serhad Soyhan, "Impact of the temperature variation on the thermal conductivity of gas diffusion layers for polymer electrolyte fuel cells," *Fuel*, vol. 345, 2023, doi: 10.1016/j.fuel.2023.128097.

[4] O. A. Towoju and F. A. Ishola, "A case for the internal combustion engine powered vehicle," in *Energy Reports*, 2020. doi: 10.1016/j.egyr.2019.11.082.

[5] A. Ozden, S. Shahgaldi, X. Li, and F. Hamdullahpur, "A review of gas diffusion layers for proton exchange membrane fuel cells—With a focus on characteristics, characterization techniques, materials and designs," *Progress in Energy and Combustion Science*, vol. 74. 2019. doi: 10.1016/j.pecs.2019.05.002.

[6] R. Omrani and B. Shabani, "Review of gas diffusion layer for proton exchange membrane-based technologies with a focus on unitised regenerative fuel cells," *International Journal of Hydrogen Energy*, vol. 44, no. 7. 2019. doi: 10.1016/j.ijhydene.2018.12.120.

[7] P. C. Okonkwo and C. Otor, "A review of gas diffusion layer properties and water management in proton exchange membrane fuel cell system," *International Journal of Energy Research*, vol. 45, no. 3. 2021. doi: 10.1002/er.6227.

[8] M. Kaplan, "Three-dimensional CFD analysis of PEMFC with different membrane thicknesses," *Renewable Energy and Sustainable Development*, vol. 8, no. 2, 2022, doi: 10.21622/resd.2022.08.2.045.

[9] mahmut kaplan, "A Numerical Parametric Study on the Impacts of Mass Fractions of Gas Species on PEMFC Performance," *SSRN Electronic Journal*, 2023, doi: 10.2139/ssrn.4222199.

[10] G. He, Y. Yamazaki, and A. Abudula, "A three-dimensional analysis of the effect of anisotropic gas diffusion layer(GDL) thermal conductivity on the heat transfer and two-phase behavior in a proton exchange membrane fuel cell(PEMFC)," *J Power Sources*, vol. 195, no. 6, 2010, doi: 10.1016/j.jpowsour.2009.09.059.

[11] I. Dincer, "Hydrogen and Fuel Cell Technologies for Sustainable Future," *Jordan Journal of Mechanical and Industrial Engineering*, vol. 2, no. 1, 2008.

[12] L. Cindrella *et al.*, "Gas diffusion layer for proton exchange membrane fuel cells-A review," *Journal of Power Sources*, vol. 194, no. 1. 2009. doi: 10.1016/j.jpowsour.2009.04.005.

[13] A. Vikram, P. R. Chowdhury, R. K. Phillips, and M. Hoorfar, "Measurement of effective bulk and contact resistance of gas diffusion layer under inhomogeneous compression - Part I: Electrical conductivity," *J Power Sources*, vol. 320, 2016, doi: 10.1016/j.jpowsour.2016.04.110.

[14] G. Athanasaki, A. Jayakumar, and A. M. Kannan, "Gas diffusion layers for PEM fuel cells: Materials, properties and manufacturing – A review," *International Journal of Hydrogen Energy*, vol. 48, no. 6. 2023. doi: 10.1016/j.ijhydene.2022.10.058.

[15] B. Hasanah, "Studi Tingkat Kerusakan Bangunan Rumah Terhadap Serangan Rayap Di Kecamatan Bankit Kabupaten Way Kanan," *Fakultas Tarbiyah Dan Keguruan IAIN Raden Intan Lampung*, 2021.

[16] N. Alhazmi, D. B. Ingham, M. S. Ismail, K. J. Hughes, L. Ma, and M. Pourkashanian, "Effect of the anisotropic thermal conductivity of GDL on the performance of PEM fuel cells," *Int J Hydrogen Energy*, vol. 38, no. 1, pp. 603–611, Jan. 2013, doi: 10.1016/j.ijhydene.2012.07.007.

[17] A. Martín-Alcántara, L. González-Morán, J. Pino, J. Guerra, and A. Iranzo, "Effect of the Gas Diffusion Layer Design on the Water Management and Cell Performance of a PEM Fuel Cell," *Processes*, vol. 10, no. 7, 2022, doi: 10.3390/pr10071395.

[18] M. Kaplan, "Numerical investigation of influence of cross-sectional dimensions of flow channels on pem fuel cell performance," *Journal of Energy Systems*, vol. 5, no. 2, 2021, doi: 10.30521/jes.871018.

[19] E. E. Kahveci and I. Taymaz, "Assessment of single-serpentine PEM fuel cell model developed by computational fluid dynamics," *Fuel*, vol. 217, 2018, doi: 10.1016/j.fuel.2017.12.073.

[20] A. Biyiko□lu and C. Ö. Alpat, "Parametric study of a single cell proton exchange membrane fuel cell for A bundle of straight gas channels," *Gazi University Journal of Science*, vol. 24, no. 4, 2011.

[21] C. Spiegel, *PEM Fuel Cell Modeling and Simulation Using Matlab*. 2008. doi: 10.1016/B978-0-12-374259-9.X5001-0.

[22] F. Barbir, *PEM fuel cells: Theory and practice*. 2012. doi: 10.1016/C2011-0-06706-6.

ACADEMY Publishing Center

RESD

Renewable Energy and Sustainable Development Journal

ISSN 2356-8569